ADVANCED OPTICAL MATERIALS
www.advopticalmat.de

Extended Range of Ratiometric Luminescence Codes with Ce^{3+} Modified $Gd_2O_2S:Er^{3+},Yb^{3+}$ Shortwave Infrared Phosphors

*Arzu Cosgun Ergene, Eduard Madirov, Elizabeth Coetsee-Hugo, Hendrik Swart, Bryce S. Richards, and Andrey Turshatov**

Lanthanide (Ln^{3+}) based luminescent materials, with their distinctive emission spectra, offer opportunities to develop novel coding patterns for various applications, including Tracer Based Sorting (TBS). TBS uses trace amounts of inorganic phosphors and is a promising method for sorting plastics based on criteria beyond plastic type. This study investigates the synergistic effect of co-doping with Ce^{3+} to enhance Er^{3+} luminescence at ≈1550 nm (with a maximum photoluminescence quantum yield (PLQY) of 5.7%) while significantly reducing Yb^{3+} luminescence at ≈1000 nm. The underlying mechanisms of these properties are analyzed using absolute PLQY measurements in an integrating sphere, luminescence decay studies, and X-ray photoelectron spectroscopy. Hyperspectral shortwave infrared imaging reveals an extended range of unique tracer combinations based on ratiometric intensity measurements, particularly when the $Yb^{3+}/Er^{3+}/Ce^{3+}$ tracers are mixed with a single-doped Yb^{3+} tracer, compared to simple mixtures of Ce^{3+}-free Yb^{3+}/Er^{3+} and Yb^{3+} tracers. Therefore, the use of the tri-doped $Yb^{3+}/Er^{3+}/Ce^{3+}$ Gd_2O_2S tracer increases the diversity of available luminescent tracers that may be of potential interest in the identification and sorting of plastic waste using the TBS process.

1. Introduction

Within the European plastic production industry in 2021, the utilization of circular plastic was only 12.4%, significantly far behind meeting the 2030 targets of 55%.[1,2] Current recycling technologies, such as mechanical-chemical processes, face a significant challenge in achieving widespread adoption due to the inability to achieve high purity levels from different types of plastics in sorted plastic waste.[3] Spectroscopic sorting technologies, such as near-infrared (NIR) sorting, are mainly used for sorting uncomplicated blends and polymers of similar quality.[4] NIR sorting relies on comparing the reflectance spectra of plastics within the 1000–1700 nm range (or the broader defined shortwave infrared (SWIR; 1000–2000 nm) range), illuminated by a halogen lamp. However, such technologies have limitations in dealing with black plastics and also distinguishing identical polymer types, that are employed for different applications, one example being polyethylene terephthalate (PET) for either food packaging or personal care products.[5] To enhance the circularity of plastic waste and reduce its impact on the ecosystem, there is an urgent need for high-accuracy sorting technology capable of identifying and sorting plastics based on criteria beyond plastic type.[6] We believe that the new sorting process should also address the issue of microplastic generation, which can occur in state-of-the-art sorting facilities.[7,8]

Tracer-based sorting (TBS) is an advanced identification technology that involves unique combinations of fluorescent tracers and the necessary optical excitation and detection system (see **Figure 1a**) to decode their unique emission lines.[3,9] In TBS, organic or inorganic tracers are incorporated into the polymer at trace amounts (ppm level) or applied via a printed label to create unique optical coding patterns with no adverse effects – neither on the visual appearance of the plastic object nor on its mechanical properties.[4,10,11] The potential to create novel coding patterns for the TBS process can be realized using lanthanide (Ln^{3+})-based photonic tracers, which feature unique emission spectra spanning from the visible through to the SWIR spectral region.[12] These tracers utilize inorganic microcrystals

A. Cosgun Ergene, E. Madirov, B. S. Richards, A. Turshatov
Institute of Microstructure Technology
Karlsruhe Institute of Technology
Hermann-von-Helmholtz-Platz 1, 76344 Eggenstein-Leopoldshafen, Germany
E-mail: andrey.turshatov@kit.edu
E. Coetsee-Hugo, H. Swart
Department of Physics
University of the Free State
Bloemfontein 9300, South Africa
B. S. Richards
Light Technology Institute
Karlsruhe Institute of Technology
Engesserstraße 13, 76131 Karlsruhe, Germany

The ORCID identification number(s) for the author(s) of this article can be found under https://doi.org/10.1002/adom.202400925

DOI: 10.1002/adom.202400925

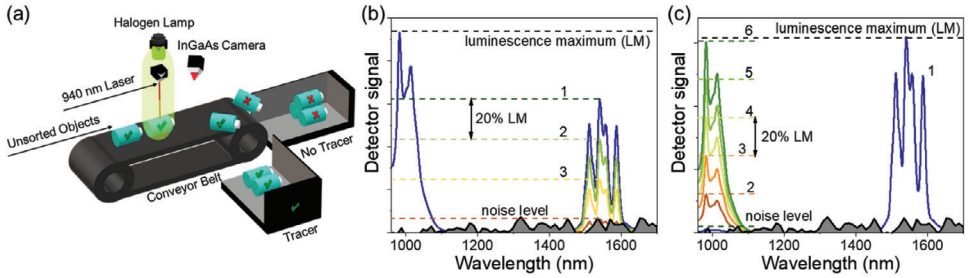

Figure 1. a) Schematic of a standard NIR sorting machine that has been enhanced so that excitation via 940 nm laser light – required for tracer-based sorting (TBS) – is also possible. The InGaAs camera measures the reflectance (R) of objects (where absorption contributes as signal R < 100%, while luminescence contributes as R > 100%) as the conveyor belt moves at speeds of at least 3 m^{-1} s. This allows objects carrying a luminescent tracer to be identified and sorted out from all the other objects via air jets (not shown). After subtraction of the background reflectance signal from the halogen lamp (which is required for standard NIR sorting), the luminescence signal from the tracers is identified as shown in b) and c). Two situations are considered: (b) a doubly-doped Er^{3+}/Yb^{3+} tracer (with 2 emission peaks at ≈1000 nm and ≈1550 nm, blue line) is mixed with a single-doped Yb^{3+} tracer (with one emission peak at ≈1000 nm). The detector is optimized for the strongest luminescent peak (≈1000 nm). The mixing of tracers leads to a reduction of the 1550 nm peak and only 3 unique combinations of tracers are possible, assuming that the difference in intensity of the 1550 nm peak should not be less than 20% of the strongest luminescent peak. (c) A doubly-doped Yb^{3+}/Er^{3+} tracer (with only one peak at 1550 nm, blue line) is mixed with a single-doped Yb^{3+} tracer. The detector is optimized for the strongest luminescent peak (≈1550 nm). The mixing of the tracers results in an increase of the 1000 nm peak and now 5 unique combinations of tracers are possible, provided that the difference in intensity of the 1000 nm peak should not be less than 20% of the strongest luminescent peak. LM stands for the luminescence maximum.

co-doped with ytterbium (Yb^{3+}) – the ion that can efficiently absorb the excitation light (976 nm) and re-emit the light at ≈1000 nm. The Yb^{3+} ion can also efficiently sensitize other Ln^{3+} ions, such as erbium (Er^{3+}), holmium (Ho^{3+}), or thulium (Tm^{3+}). These tracers exhibit both upconversion (UC) in the visible/NIR and downshifted (DS) emissions in the SWIR range when excited at a wavelength of 976 nm with a photoluminescence quantum yield (PLQY) that depends on the structural properties of the host crystal and the co-doped ions. The choice of SWIR tracers detectable in a state-of-the-art sorting machine within an operational sorting facility is limited to 3 ions: Yb^{3+} (luminescent peak at ≈1000 nm), Ho^{3+} (luminescent peak at ≈1200 nm) and Er^{3+} (luminescent peak ≈1550 nm).[12] These 3 luminescent peaks can be combined to form 7 codes ($N = 2^n$-1, where n = 3 is the number of available tracers, N = 7 is the number of codes) by mixing pure tracers. Another potential tracer, based on Tm^{3+}, emits at ≈1800 nm, slightly beyond the spectral range of the standard InGaAs detector (with the range 900–1700 nm), but may be detectable with an extended InGaAs detector (with the range 900–2500 nm) in the future. It is therefore imperative to expand the repertoire of luminescent codes, for example by using the ratiometric SWIR codes discussed in this study.

Among other inorganic host crystals, lanthanide oxysulfides have been extensively studied for their wide applications in luminescent devices,[13] photonics, display devices, lasers, afterglow,[14] and biological imaging[15] due to their unique characteristics arising from their *f-f* and *f-d* electronic transitions.[16] Of these, Gd_2O_2S stands out as an efficient host with favourable chemical and physical properties, including good chemical stability, lack of moisture sensitivity, low crystal symmetry (facilitating radiative processes in Ln^{3+} ions), non-toxicity, low phonon energies (~440 cm^{-1}),[17,18] and a wide band gap of 4.2–4.8 eV (providing a colourless tracer).[15,19–21] The presence of Gd^{3+} as the core ion makes Gd_2O_2S a suitable host for various Ln^{3+} doping ions, allowing the creation of a range of phosphors that emit over a wide range of wavelengths. The most used Ln^{3+} dopant combinations for UC and DS of Gd_2O_2S phosphors involve Er^{3+} and Yb^{3+} ions. Yb^{3+} ions serve as efficient sensitizers to enhance the population of excited Er^{3+} ions due to the large absorption cross section at 980 nm[22,23] and thanks to the close proximity of the Yb^{3+}:$^2F_{5/2}$ level to the Er^{3+}:$^4I_{11/2}$ level, facilitating good energy transfer (ET) at 980 nm.[20–24]

In many hosts, regardless of phonon energy, strong visible UC emission and back energy transfer (BET) Er^{3+}:$^4I_{11/2}$→Yb^{3+}:$^2F_{5/2}$ occur due to the long fluorescence lifetime of the Er^{3+}:$^4I_{11/2}$ level.[25,26] This results in incomplete quenching of Yb^{3+}:$^2F_{5/2}$ →$^2F_{7/2}$ emission (i.e., photoluminescence from this level is still observed) and a decrease in the nonradiative decay rate from the $^4I_{11/2}$ to $^4I_{13/2}$ levels, ultimately weakening the 1550 nm emission band.[5,27,28] To enhance the 1550 nm emission, it is crucial to reduce the Er^{3+} population lifetime at the $^4I_{11/2}$ level and then accelerate a rapid non-radiative transition from the $^4I_{11/2}$ level to the $^4I_{13/2}$ level.[27,29]

For TBS, Er^{3+},Yb^{3+}-doped tracers with unique emission lines can be combined to create unique multiple codes. However, the presence of 2 emission lines at ≈1000 nm and ≈1550 nm reduces the uniqueness of luminescent tracers when multiple codes are generated by the simple mixing of 2 tracers. The idea that mixing the Yb^{3+}/Er^{3+} tracer (showing unquenched Yb^{3+} luminescence (≈1000 nm) as well as Er^{3+} emission (≈1550 nm)) with the single-doped Yb^{3+} tracer allows fewer unique combinations compared to using the Yb^{3+}/Er^{3+} tracer (showing no Yb^{3+} luminescence (≈1000 nm) and only Er^{3+} emission (≈1550 nm)) is illustrated in Figure 1b,c. Figure 1b demonstrates a scenario where the Yb^{3+}/Er^{3+} tracer has these 2 emission peaks at ≈1000 nm and ≈1550 nm, and the tracer quantity is arbitrary and chosen to exhibit the strongest luminescence (without saturation of a spectrometer). The spectra in the figure are normalized to the Yb^{3+} intensity ≈1000 nm. When the single-doped Yb^{3+} tracer is added to this doubly-doped Yb^{3+}/Er^{3+} tracer, the intensity of the Er^{3+} peak (≈1550 nm) decreases, provided that the intensity

of the Yb^{3+} peak (≈1000 nm) remains constant. Assuming that the Er^{3+} peak (≈1550 nm) decreases by a step of 20% of the strongest luminescence, only 3 unique combinations (marked 1–3 in Figure 1b) of tracer are possible. In contrast, starting with the Yb^{3+}/Er^{3+} tracer, which shows no Yb^{3+} luminescence (Figure 1c, the spectra are normalized to the Er^{3+} intensity ≈1550 nm.), allows the amount of tracer to be optimized for the strongest luminescence for the 1550 nm peak. It is worth noting that a single-doped Er^{3+} tracer cannot be used due to the weak absorption of Er^{3+} at 976 nm. Furthermore, when the doubly-doped Yb^{3+}/Er^{3+} tracer with quenched Yb^{3+} luminescence is mixed with a single-doped Yb^{3+} tracer, the intensity of the 1000 nm peak gradually increases in steps of 20% of the strongest luminescence, allowing the creation of 5 unique mixtures (marked 2–6 in Figure 1c) plus the doubly-doped Yb^{3+}/Er^{3+} tracer itself (marked 1 in Figure 1c) – twice as many combinations as when using the Yb^{3+}/Er^{3+} tracer with unquenched Yb^{3+} luminescence.

The synthesis of a new Yb^{3+}/Er^{3+} tracer with quenched Yb^{3+} luminescence and high PLQY is therefore crucial, although not a trivial task. In the past, researchers have explored the incorporation of suitable co-dopant ions, such as Ce^{3+}, into glass and crystalline hosts to enhance the non-radiative relaxation process of the $^4I_{11/2}$-$^4I_{13/2}$ transition.[25–27,29–38] This enhancement aims to improve the 1550 nm fluorescence intensity via ET from Er^{3+} to Ce^{3+} ions (Er^{3+}:$^4I_{11/2}$ + Ce^{3+}:$^2F_{5/2}$ → Er^{3+}:$^4I_{13/2}$ + Ce^{3+}:$^2F_{7/2}$).[29,32] The absorption peak of Ce^{3+}:$^2F_{5/2}$ → $^2F_{7/2}$ transition is ≈2300 cm^{-1}, while the energy gap between the Er^{3+}:$^4I_{11/2}$-$^4I_{13/2}$ emission transition is ≈3200–3500 cm^{-1}.[27,38] Therefore, the release of additional phonons of the host is crucial to compensate for this energy mismatch, promoting ET from Er^{3+}:$^4I_{11/2}$ to Ce^{3+}:$^2F_{7/2}$ levels.[27]

In this study, we explore the synergistic effect of co-doping with Ce^{3+} on achieving strong Er^{3+} luminescence at ≈1550 nm while minimizing Yb^{3+} luminescence at ≈1000 nm. Through comprehensive structural and optical characterization, we elucidate the underlying mechanism driving these luminescence properties. In addition, we demonstrate the advantages of using such a tracer through hyperspectral SWIR imaging and highlight its potential for creating novel tracer combinations by mixing with a single-doped Yb^{3+} tracer that emits only at ≈1000 nm. The method presented significantly increases the pool of luminescent tracers, thereby enhancing the effectiveness of TBS in separating polymer waste into numerous fractions aligned to precise polymer specifications.

2. Results and Discussion

The selection of optimal doping concentrations for Yb^{3+} and Er^{3+} ions to achieve robust SWIR luminescence at ≈1550 nm in the Er^{3+}:$^4I_{13/2}$ state is based on several key considerations. First, the concentration of Yb^{3+} must strike a balance between effective sensitization and minimizing concentration quenching of the Yb^{3+}:$^2F_{5/2}$ state. Kumar et al. have previously shown that an ideal Yb^{3+} concentration for sensitizing UC luminescence in Y_2O_2S:Er^{3+},Yb^{3+} phosphors is in the range of 8–14 mol.%.[39] Conversely, the reported optimum Er^{3+} concentration for UC is much lower, typically ≈1 mol.%, mainly due to the pronounced cross-relaxation phenomena of the Er^{3+}:$^4S_{3/2}$ state. The likelihood of cross-relaxation events increases with higher Er^{3+} concentrations, leading to a reduction in UC intensity. However, for 1550 nm DS luminescence of Er^{3+} under 976 nm excitation, cross-relaxation effects are minimal, allowing a higher concentration of Er^{3+} to be utilized. For example, Madirov et al.[40] demonstrated the remarkable PLQY at ≈1550 nm in BaF_2:Er^{3+} crystals, achieving significant emission at Er^{3+} concentrations approaching 5–10 mol.% (in the case of the excited Er^{3+}:$^4F_{9/2}$ state). Based on these findings, we chose doping concentrations of 6 mol.% for Er^{3+} and 14 mol.% for Yb^{3+}. This choice was made with the understanding that while extensive combinatorial optimization of doping concentrations could potentially yield slightly higher PLQY of 1550 nm luminescence, our chosen concentrations are close to the optimal balance for maximizing luminescence efficiency.

2.1. Material Properties

The X-ray diffraction (XRD) patterns of Gd_2O_2S:$6Er^{3+}$,$14Yb^{3+}$, $x$$Ce^{3+}$ are shown in **Figure 2a**. All samples exhibit well-crystallised structures that match the standard pattern of Gd_2O_2S (PDF 04-002-8121), with no additional peaks indicating that no impurity phases were detectable via XRD. As the concentration of Ce^{3+} dopant increases, the positions of the peaks shift toward lower angles, implying the incorporation of dopants into the host lattice (Figure S1, Supporting Information). To investigate the impact of Ce^{3+} doping on the crystalline structure of Gd_2O_2S, Rietveld structural refinement analysis was performed on the XRD data (Figure S2, Supporting Information).

The crystal structure of Gd_2O_2S belongs to the hexagonal crystal system, with the trigonal space group $P\bar{3}m1$ (164). The theoretical lattice parameters are a = b = 3.855 Å, c = 6.667 Å, $\alpha = \beta = 90°$, $\gamma = 120°$. As seen in Figure 2b the crystal structure comprises one Gd1 site with C_{3v} symmetry, coordinated by 4 oxygen atoms and 3 sulfur atoms. The dopant ions replace the host Gd^{3+} ions at the 2d site, resulting in a seven-coordinated geometry.[22,23]

Changes in the lattice parameters with the addition of dopant ions were calculated through Rietveld refinement and are presented in Table S1 (Supporting Information). These parameters were then compared against those of Gd_2O_2S:$6Er^{3+}$,$14Yb^{3+}$. Figure 2c illustrates that the refined unit-cell parameters exhibit an expansion in the Gd_2O_2S:$6Er^{3+}$,$14Yb^{3+}$ crystal lattice dimensions (a, b, c, and volume) due to the larger ionic radius of Ce^{3+} (1.07 Å) as compared to the ionic radii of the Er^{3+} (0.945 Å), Yb^{3+} (0.925 Å), and Gd^{3+} (1.00 Å) ions for 7 coordination.[41] The actual concentration of Ce^{3+} within the host was determined using X-ray fluorescence spectroscopy (XRF) (Table S2, Supporting Information).

The particle size and morphology of Gd_2O_2S:$6Er^{3+}$,$14Yb^{3+}$, $x$$Ce^{3+}$, were characterized using a scanning electron microscope (SEM). Microcrystalline particles were observed in **Figure 3a**. The particle size and morphology showed no significant changes with the addition of Ce^{3+} ions, and the average particle size remained in the range of µm (Figure S3, Supporting Information). Energy dispersive X-ray spectroscopy (EDX) elemental analysis applied to Gd_2O_2S:$6Er^{3+}$,$14Yb^{3+}$,$0.2Ce^{3+}$ sample (Figure 3a) reveals homogeneous distributions of dopant ions, suggesting successful doping within the host structure as seen in Figure 3b,c.

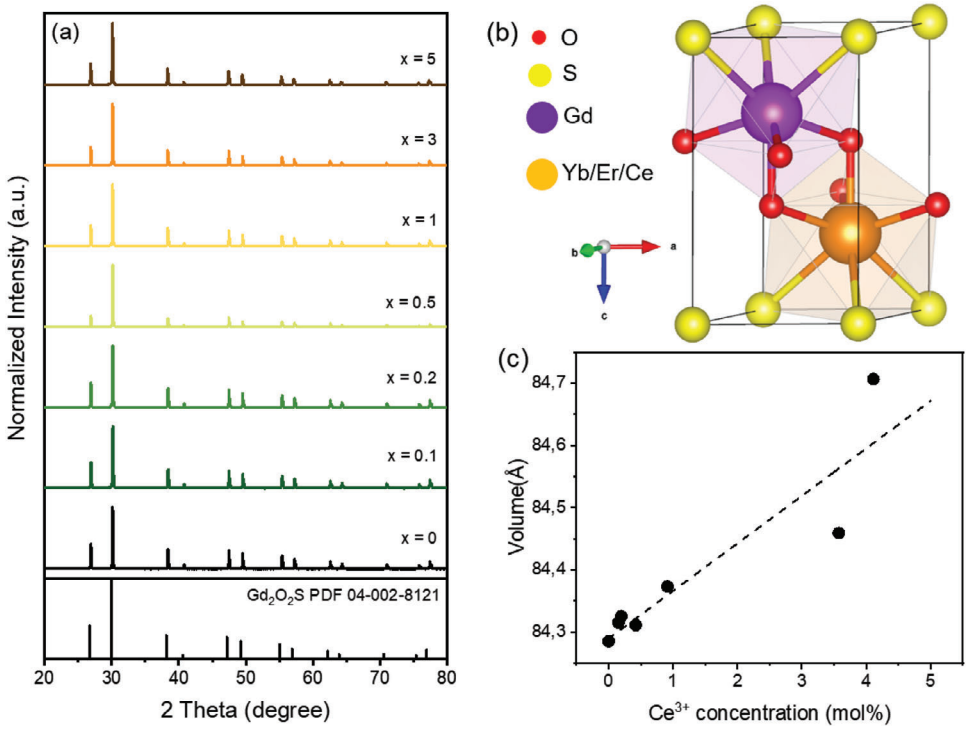

Figure 2. a) X-ray diffractograms of Gd_2O_2S:$6Er^{3+}$,$14Yb^{3+}$,xCe^{3+}; b) crystalline structure of Gd_2O_2S lattice showing with dopant ions; c) Volume changes resulting from modification by Ce^{3+} in Gd_2O_2S:$6Er^{3+}$,$14Yb^{3+}$, xCe^{3+}.

2.2. Optical Properties

Figure 4a,b show the absorption of the investigated samples. Samples that contain Yb^{3+} ions have the most prominent peak at ≈1000 nm. It originates from the $^2F_{7/2}$ – $^2F_{5/2}$ transition of the Yb^{3+} ions. The peak is relatively broad ranging from 910 to 1030 nm. It can be noticed that the introduction of the Ce^{3+} ions leads to a certain decrease in the absorption intensity of Yb^{3+} band. However, this is only prominent in samples with relatively high amounts of Ce^{3+} (>0.5 mol.%). In subsequent

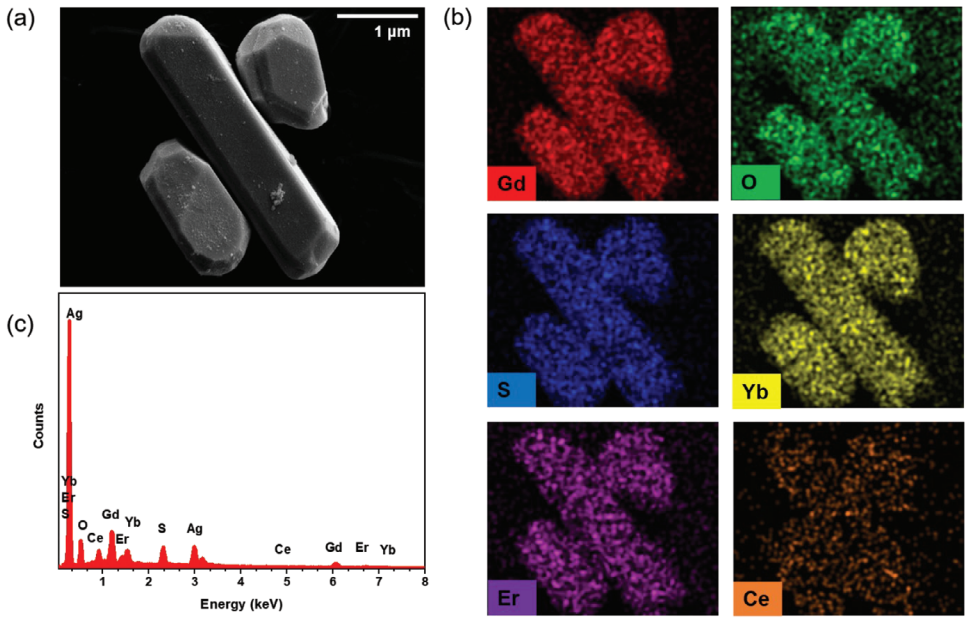

Figure 3. a) SEM image of a Gd_2O_2S:$6Er^{3+}$,$14Yb^{3+}$,$0.2Ce^{3+}$ representative sample; b) EDX elemental maps of the corresponding elements of the Gd_2O_2S:$6Er^{3+}$,$14Yb^{3+}$,$0.2Ce^{3+}$ sample; c) EDX spectrum of the Gd_2O_2S:$6Er^{3+}$,$14Yb^{3+}$,$0.2Ce^{3+}$ sample.

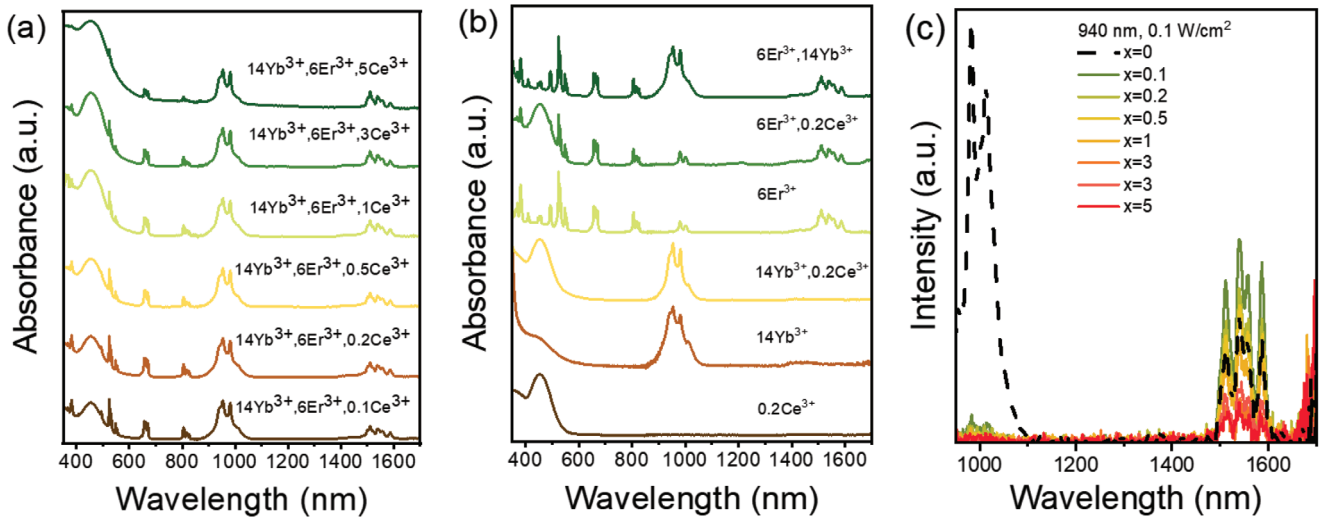

Figure 4. a) Absorption spectra of Gd_2O_2S:6Er^{3+},14Yb^{3+}, xCe^{3+} samples; b) Absorption spectra of Gd_2O_2S samples co-doped with different combinations of Er^{3+}, Yb^{3+} and Ce^{3+}; c) Luminescence spectra of Gd_2O_2S:6Er^{3+},14Yb^{3+}, xCe^{3+} samples excited using a 940 nm laser with intensity of 0.1 W cm^{-2}.

experiments, 2 laser sources emitting at wavelengths of 940 and 976 nm were used to generate SWIR luminescence. It was hypothesized that the 940 nm laser could selectively excite Yb^{3+} ions, while the 976 nm laser could excite both Yb^{3+} and Er^{3+} ions in Yb^{3+}/Er^{3+} co-doped samples. Samples that have Er^{3+} ions have intense absorption peaks at ≈520 nm (Er^{3+}: $^2I_{15/2} - {}^2H_{11/2}$), ≈650 nm ($Er^{3+}$: $^2I_{15/2} - {}^4F_{9/2}$), ≈800 nm (Er^{3+}: $^2I_{15/2} - {}^4I_{9/2}$) and ≈1550 nm (Er^{3+}: $^2I_{15/2} - {}^4I_{13/2}$). The addition of Ce^{3+} manifests in the appearance of a wide absorption band centered ≈450 nm (Ce^{3+}: 4f–5d).

Using a strong absorption band of Yb^{3+} (930–1000 nm) the DS luminescence of the Er^{3+}:$^4I_{13/2}$ state (Figure 4c) can be obtained as depicted in **Figure 5**.

Figure 4c shows the luminescence of the Gd_2O_2S:6Er^{3+},14Yb^{3+} sample under 940 nm excitation with 2 distinct peaks observed at ≈1000 and ≈1550 nm. These peaks are attributed to the radiative transitions from the Yb^{3+}:$^2F_{5/2}$&Er^{3+}:$^4I_{11/2}$ manifold and Er^{3+}:$^4I_{13/2}$ states to the ground state, respectively. Accordingly, the PLQY values for these peaks are measured to be 11.5% and 3.5%. A significant effect is observed upon the addition of 0.1 and 0.2 mol.% Ce^{3+} to the Gd_2O_2S:6Er^{3+},14Yb^{3+} sample. The luminescence peak at ≈1000 nm is strongly quenched, while the luminescence at ≈1550 nm is enhanced (PLQY = 5.7%, as seen in **Figure 6a**), resulting in a luminescent material with a single peak within the detection range of the InGaAs detector (1000–1800 nm).

Figure 6a illustrates that the effect of Ce^{3+} on enhancing or depleting 1550 nm luminescence (under 940 nm excitation) depends on the excitation intensity. For example, at a low excitation intensity of 0.1 W/cm^2, co-doping with Ce^{3+} (0.1 and 0.2 mol.%) leads to an increase in PLQY from 3.5% (for Ce^{3+}-free samples) to 5.7%. Conversely, at an excitation intensity of 2 W cm^{-2}, the PLQY of the 1550 nm emission decreases from 5.9% (for Ce^{3+}-free samples) to 3% for the Gd_2O_2S:6Er^{3+},14Yb^{3+},0.1Ce^{3+} and Gd_2O_2S:6Er^{3+},14Yb^{3+},0.2Ce^{3+} samples. Moreover, with increasing Ce^{3+} concentration, the depletion of the 1550 nm emission intensifies, reaching the lowest PLQY of 0.8% (at 2 W cm^{-2}) for the Gd_2O_2S:6Er^{3+},14Yb^{3+},5Ce^{3+} sample.

In order to fully understand the effect of Ce^{3+} on the luminescence of Er^{3+}, we have meticulously quantified every step of the Yb^{3+}:$^2F_{5/2}$ → Er^{3+}:$^4I_{11/2}$ → Er^{3+}:$^4I_{13/2}$ → Er^{3+}:$^4I_{15/2}$ process (Figure 5). For clarity, we will use the term "$PLQY_{i\to g}$ (%)" to quantify the radiative transition between an excited state (*i*) and a ground state (*g*). Here, PLQY represents the ratio between the number of emitted and absorbed photons. Additionally, we will use "Efficiency – $\phi_{i\to j}$ (%)" to denote the transitions between excited states. In this context, ϕ indicates the contribution of the transition from one excited state (*i*) to another excited state (*j*)

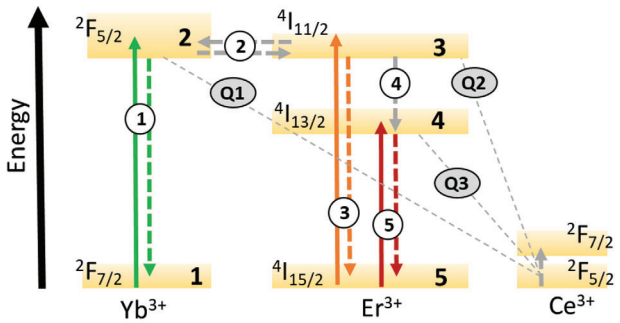

Figure 5. Schematic of energy states of Yb^{3+}, Er^{3+}, and Ce^{3+}. Overall, the process DS emission at ≈1550 nm starts from excitation of the Yb^{3+}:$^2F_{5/2}$ state ①, subsequent ET to Er^{3+}:$^4I_{11/2}$ state ②, which can be reversible due to little energy difference, subsequent radiative and non-radiative transition to the Er^{3+}:$^4I_{13/2}$ state ④ and radiative relaxation to the ground state Er^{3+}:$^4I_{15/2}$ ⑤. The question arises: How does Ce^{3+} influence the relaxation of Yb^{3+}:$^2F_{5/2}$ (Q1), Er^{3+}:$^4I_{11/2}$ (Q2) and Er^{3+}:$^4I_{13/2}$ (Q3) states? In order to answer this question, the luminescence of Er^{3+}:$^4I_{11/2}$ ③ and Er^{3+}:$^4I^{3/2}$ ⑤ can be probed under direct excitation of these states. The electronic states have been numbered (1-5) for the convenience of the reader in the text explanations.

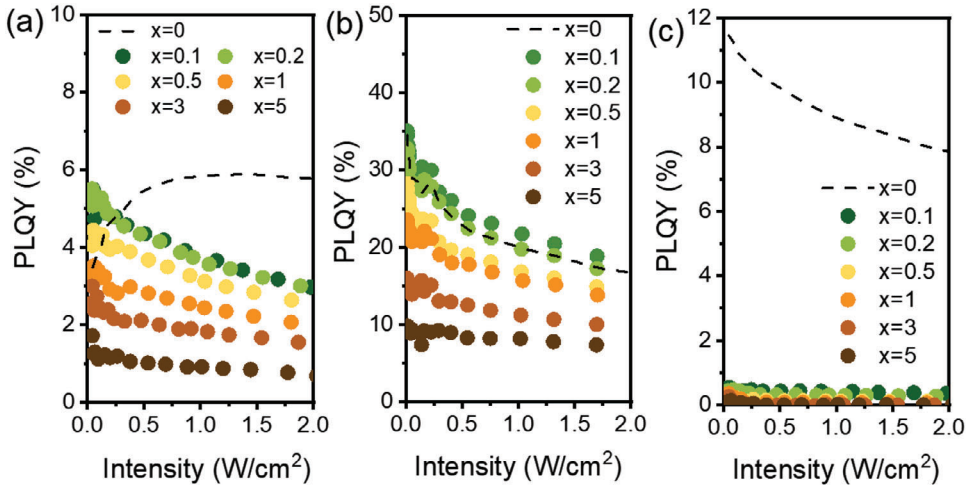

Figure 6. PLQY of $Gd_2O_2S:6Er^{3+},14Yb^{3+},xCe^{3+}$ samples: a) PLQY of Er^{3+}:$^4I_{13/2}$-$^4I_{15/2}$ emission ($PLQY_{4\rightarrow5}$, integration range 1520–1650 nm) as a function of excitation intensity under excitation at 940 nm; b) $PLQY_{4\rightarrow5}$ (integration range 1520–1650 nm) as a function of excitation intensity under excitation at 1510 nm; c) PLQY of Er^{3+}:$^4I_{11/2}$-$^4I_{15/2}$&Yb^{3+}:$^2F_{5/2}$-$^2F_{7/2}$ emission ($PLQY_{2\rightarrow1}$, integration range 950–1050 nm) as a function of excitation intensity under excitation at 940 nm. The size of the dots is representative of the uncertainty.

expressed as a percentage relative to all other deactivation pathways of state (*i*).

The PLQY of Er^{3+}:$^4I_{13/2}$ – $^4I_{15/2}$ transition ($PLQY_{4\rightarrow5}$) can be determined by direct excitation of the Er^{3+}:$^4I_{13/2}$ state. Figure 6b shows the $PLQY_{4\rightarrow5}$ emission when excited by a 1510 nm laser. The highest PLQY of 35% is observed for Ce^{3+} free samples at low excitation intensity of 0.01 W/cm². The PLQY decreases with both increasing excitation intensity and Ce^{3+} concentration (>0.5% Ce^{3+}). **Figure** 7a,b shows the $PLQY_{4\rightarrow5}$ values in the additional Yb^{3+}-free samples, $Gd_2O_2S:6Er^{3+}$, xCe^{3+} under 976 nm and 1510 nm excitation, respectively. The analysis of Figures 6a and 7a indicates that co-doping with Yb^{3+} leads to a reduction in $PLQY_{4\rightarrow5}$ (at excitation 940 and 976 nm). This decrease can be attributed to the introduction of additional relaxation pathways associated with Yb^{3+} ions, including radiative relaxation, exciting state migration, and quenching. In summarizing the findings from Figures 6b and 7b, it can be inferred that neither Yb^{3+} (14 mol.%) nor Ce^{3+} (0.1 and 0.2 mol.%) co-doping significantly impacts the $PLQY_{4\rightarrow5}$ (at excitation 1510 nm) in the $Gd_2O_2S:6Er^{3+},14Yb^{3+}$, xCe^{3+} sample when compared to the $Gd_2O_2S:6Er^{3+}$, xCe^{3+} samples. However, with a further increase in Ce^{3+} concentration (0.5–5 mol.%), there is a notable quenching effect observed on the Er^{3+}:$^4I_{13/2}$ state for both series. This is evident from the decrease in $PLQY_{4\rightarrow5}$ (at excitation 1510 nm) across all excitation intensities and Ce^{3+} concentrations (0.5–5 mol.%).

In addition, Figure 6c confirms the observation reported in Figure 4c. The introduction of Ce^{3+} as a co-dopant results in a notable decrease in $PLQY_{2\rightarrow1}$ (1000 nm emission) which drops from 11.5% down to 0.7% for the lowest Ce^{3+} concentration of

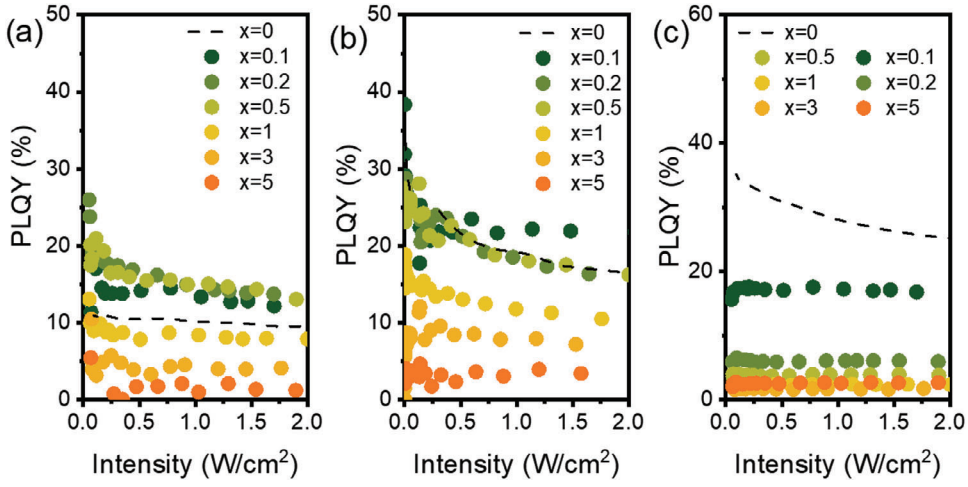

Figure 7. PLQY of $Gd_2O_2S:6Er^{3+},xCe^{3+}$ samples: a) PLQY of Er^{3+}:$^4I_{13/2}$-$^4I_{15/2}$ emission ($PLQY_{4\rightarrow5}$, integration range 1520–1650 nm) as a function of excitation intensity under excitation at 976 nm; b) $PLQY_{4\rightarrow5}$ (integration range 1520–1650 nm) as a function of excitation intensity under excitation at 1510 nm; c) PLQY Er^{3+}:$^4I_{11/2}$-$^4I_{15/2}$ emission ($PLQY_{3\rightarrow5}$ integration range 980–1050 nm) as a function of excitation intensity under excitation at 976 nm. The size of the dots is representative of the uncertainty.

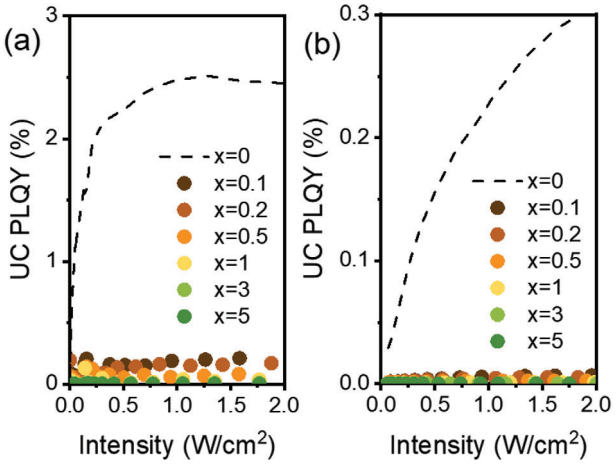

Figure 8. a) UC PLQY in Gd_2O_2S:6Er^{3+},14Yb^{3+}, xCe^{3+} samples as a function of excitation intensity under 1510 nm excitation. The UC is integrated in the range 950–1050 nm; b) UC PLQY of TA-UC in Gd_2O_2S:6Er^{3+},14Yb^{3+}, xCe^{3+} samples as a function of excitation intensity under 940 nm excitation. The UC is integrated in the range 500–700 nm. The size of the dots is representative of the uncertainty.

0.1%. This value continues to decrease with increasing Ce^{3+} concentration.

It is noteworthy that when the Gd_2O_2S:6Er^{3+},14Yb^{3+} sample is excited with a 1510 nm laser, a remarkably efficient (similar to reported by Machado et al.)[24] energy transfer upconversion (ETU) occurs, resulting in emission at ≈1000 nm (as shown in **Figure** 8a; Figure S4a, Supporting Information). This UC phenomenon can be observed even at low excitation intensities (0.005 W/cm^2) and becomes more pronounced as the intensity rises from 0.005 to 2 W cm^{-2}.

A comparison of the PLQY trend, as shown in Figure 6b, with the UC PLQY trend shown in Figure 8a, reveals a contrasting behavior between DS and UC luminescence within the same intensity range. This observation suggests that the decrease in DS intensity shown in Figure 6b with rising excitation intensity is due to an increasing contribution from the UC process. Although the ETU effect is less pronounced in Ce^{3+} doped samples (as shown in Figure 8a), this discrepancy is not due to a less efficient ETU process between the Er^{3+}:$^4I_{13/2}$ states per se, but rather to the quenching of the Er^{3+}:$^4I_{11/2}$ state.

In the next stage of the analysis, the efficiency of the Er^{3+}:$^4I_{11/2}$ – $^4I_{13/2}$ transition ($\phi_{3\rightarrow4}$) is evaluated. In the simplest scenario, ignoring the contribution of the UC process, the efficiency $\phi_{3\rightarrow4}$ can be determined by measuring the $PLQY_{4\rightarrow5}$ under excitation of the Er^{3+}:$^4I_{11/2}$ (976 nm) and Er^{3+}:$^4I_{13/2}$ (1510 nm) states:

$$\phi_{3\rightarrow4} = \frac{PLQY_{4\rightarrow5,\ \lambda_{ex}=976nm}}{PLQY_{4\rightarrow5,\ \lambda_{ex}=1510nm}} \quad (1)$$

Equation 1 can be applied with confidence only to Gd_2O_2S:6Er^{3+} and Gd_2O_2S:6Er^{3+}, xCe^{3+} samples at low excitation intensities (specifically chosen in the calculation as 0.1 W cm^{-2} for 976 nm and 0.01 W cm^{-2} for 1510 nm). The variance in excitation intensity results in a similar number of excited Er^{3+}:$^4I_{13/2}$ states and a low and comparable contribution of ETU, increasing the reliability of the analysis.

Strong changes in the efficiency of the transition between Er^{3+}:4$I_{11/2}$ and Er^{3+}:$^4I_{13/2}$ states ($\phi_{3\rightarrow4}$) were found with Equation 1 for the Ce^{3+}-free and Ce^{3+}-co-doped samples (**Figure** 9a). The $\phi_{3\rightarrow4}$ efficiency increases from 27% (for Ce^{3+}-free sample) up to 83% for the sample with 0.2 mol. % Ce^{3+}) and then decreases with the increase of Ce^{3+} concentration.

As it has been shown in Figure 7c, the presence of Ce^{3+} significantly quenches the Er^{3+}:$^4I_{11/2}$ state, as evidenced by a decrease in $PLQY_{3\rightarrow5}$ from 35% for the Ce^{3+}-free sample to 6% for the representative sample containing 0.2 mol.% Ce^{3+}. Simultaneously, the lifetime of the Er^{3+}:$^4I_{11/2}$ state decreases from 2.4 to 0.2 ms in the presence of Ce^{3+} (as shown in Figure 9b). There is a simple relationship between PLQY and the decay time of Er^{3+}:$^4I_{11/2}$ state, which allows the rate of the radiative transition to be estimated:

$$k_r\beta = \frac{PLQY}{\tau} \quad (2)$$

Where β is the so-called branching ratio between Er^{3+}:$^4H_{11/2}\rightarrow{}^4H_{13/2}$ and Er^{3+}:$^4H_{11/2}\rightarrow{}^4H_{15/2}$ transitions, which can be calculated using Judd-Ofelt theory.

Using this Equation 2, the values of $k_r\beta$ = 0.10 ms^{-1} and 0.09 ms^{-1} were obtained for the Ce^{3+}-free and Ce^{3+}-co-doped samples, respectively. Since the branching ratio β for Er^{3+} is usually in the range 0.82–0.89 for a very wide range of the hosts (calculated using Judd-Ofelt theory for sulfide glasses,[42] fluorides,[43] and garnets[44]) and is normally unaffected by the host and doping concentration, this suggests that Ce^{3+} co-doping has a minimal effect on the radiative rate of the Er^{3+}:$^4I_{11/2}$-$^4I_{15/2}$ transition.

As Ce^{3+} doesn´t change the radiative rate of the Er^{3+}:$^4H_{11/2}$ state, the most plausible mechanism for the enhancement of $\phi_{3\rightarrow4}$ in the presence of Ce^{3+} involves phonon-assisted resonance energy transfer[45–47]: Er^{3+}:$^4I_{11/2}$ + Ce^{3+}:$^2F_{5/2}$ → Er^{3+}:$^4I_{13/2}$ + Ce^{3+}:$^2F_{7/2}$. The phonon assistance is needed due to a mismatch in the energy gap between Er^{3+}:$^4I_{11/2}$ and Er^{3+}:$^4I_{13/2}$ (≈3200–3500 cm^{-1}), which exceeds the energy gap of ≈2300 cm^{-1} between the Ce^{3+}:$^2F_{5/2}$ states. Consequently, the phonon-assisted resonance energy transfer requires the simultaneous release of ≈900–1200 cm^{-1} of energy, which can be achieved by the involvement of 2 to 3 phonons (with maximum phonon energy of ≈440 cm^{-1} in Gd_2O_2S) taking also into account energy distribution of phonon quanta observed in the Raman spectrum of Gd_2O_2S (Figure S5, Supporting Information).

In contrast to Yb^{3+}-free samples where the Er^{3+}:$^4I_{11/2}$ state can be selectively excited due to distinct absorption peaks (Figure 4a,b), the Er^{3+}:$^4I_{11/2}$ state is not selectively excited in Yb^{3+} and Er^{3+} co-doped samples as the absorption peaks of Er^{3+} and Yb^{3+} coincide at 976 nm. Therefore, the straightforward estimation of $\phi_{3\rightarrow4}$ in Gd_2O_2S:6Er^{3+},14Yb^{3+}, xCe^{3+} samples is, unfortunately, not possible. It is only possible to assess overall efficiency $\phi_{(2\rightarrow4)}$, which represents the excited state energy flow from the Yb^{3+}:$^2F_{5/2}$ state through the Er^{3+}:$^4I_{11/2}$ state to the Er^{3+}:$^4I_{13/2}$ state, using Equation 3:

$$PLQY_{4\rightarrow5,\ \lambda_{ex}=940nm} = \phi_{(2\rightarrow4)}\ PLQY_{4\rightarrow5,\ \lambda_{ex}=1510nm} \quad (3)$$

8c Figure 9c indicates that $\phi_{(2\rightarrow4)}$ate is independent of the Ce^{3+} concentration. It can be assumed that after excitation of the Yb^{3+}

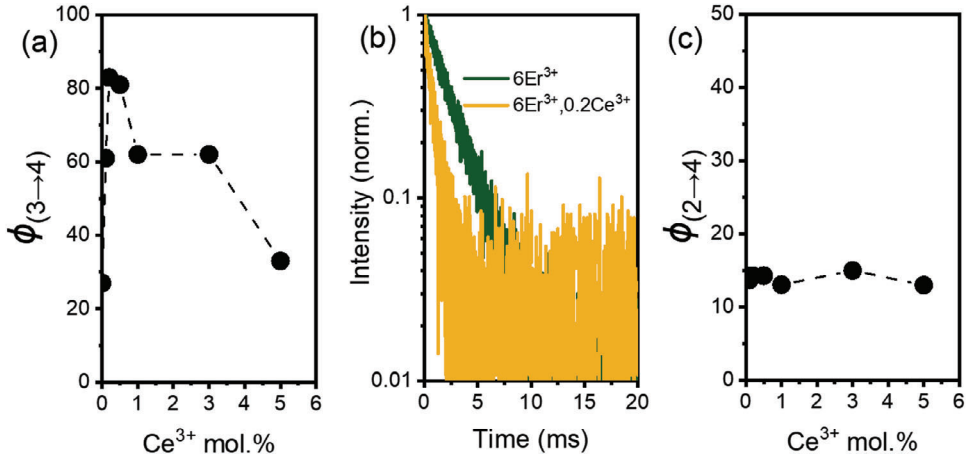

Figure 9. a) Decays of Er^{3+}:$^4I_{11/2}$ state in Gd_2O_2S:$6Er^{3+}$ and Gd_2O_2S:$6Er^{3+}$,$0.2Ce^{3+}$ samples; b) Efficiency of Er^{3+}:$^4I_{11/2}\rightarrow{}^4I_{13/2}$ transition ($\phi_{3\rightarrow4}$) as a function of Ce^{3+} concentration in Gd_2O_2S:$6Er^{3+}$,$x$$Ce^{3+}$ samples; c) Overall efficiency of Yb^{3+}:$^2F_{5/2}\rightarrow Er^{3+}$:$^4I_{13/2}$ transition ($\phi_{2\rightarrow4}$) as a function of Ce^{3+} concentration in Gd_2O_2S:$6Er^{3+}$,$14Yb^{3+}$,$x$$Ce^{3+}$ samples.

ions there is diffusion of the excited state by ET between the Yb^{3+} ions until they meet a quenching center.[48] The strong reducing conditions and CeO_2(Ce^{4+}) as a Ce-source used in the synthesis of Gd_2O_2S:Er^{3+}, Yb^{3+}, Ce^{3+} result in both electronic defects – Yb^{2+}, Ce^{4+} – and crystal structure defects that quench the Yb^{3+} excited states before radiative relaxation. However, in the presence of Er^{3+} the energy transfer $Yb^{3+}\rightarrow Er^{3+}$ is much faster than the energy migration $Yb^{3+}\rightarrow Yb^{3+}$, so the efficiency of the ET and the subsequent Er^{3+}:$^4I_{13/2}$-$^4I_{11/2}$ transition is almost independent of the amount of defects formed in the presence of different amounts of Ce.

Several interesting remarks can be additionally made with the help of model samples – Gd_2O_2S:$14Yb^{3+}$ and Gd_2O_2S:$14Yb^{3+}$,$0.2Ce^{3+}$. Even when a small amount of Ce^{3+} is added, resulting in Gd_2O_2S:$14Yb^{3+}$,$0.2Ce^{3+}$ sample, it leads to very strong quenching of Yb^{3+}:$^2F_{5/2}$ state with quenching efficiency (ϕ_Q) of 99% calculated using data from **Figure 10a** and Equation 4:

$$\phi_Q = 1 - \frac{PLQY_{2\rightarrow1,14Yb3+,0.2Ce3+}}{PLQY_{2\rightarrow1,14Yb3+}} \quad (4)$$

where, $PLQY_{2\rightarrow1,14Yb3+}$ – PLQY of Gd_2O_2S:$14Yb^{3+}$ sample under 940 nm excitation and intensity of 0.1 W cm^{-2} and $PLQY_{2\rightarrow1,14Yb3+,0.2Ce3+}$ – PLQY of Gd_2O_2S:$14Yb^{3+}$,$0.2Ce^{3+}$ sample under 940 nm excitation and intensity of 0.1 W cm^{-2}.

However, the strong quenching effect, which could potentially hinder the ET from Yb^{3+}:$^2F_{5/2}$ to Er^{3+}:$^4I_{11/2}$ in the Gd_2O_2S:$6Er^{3+}$,$14Yb^{3+}$, $x$$Ce^{3+}$ sample, does not seem to be the case, as significant emission from the Er^{3+}:$^4I_{13/2}$ state is still observed in these samples.

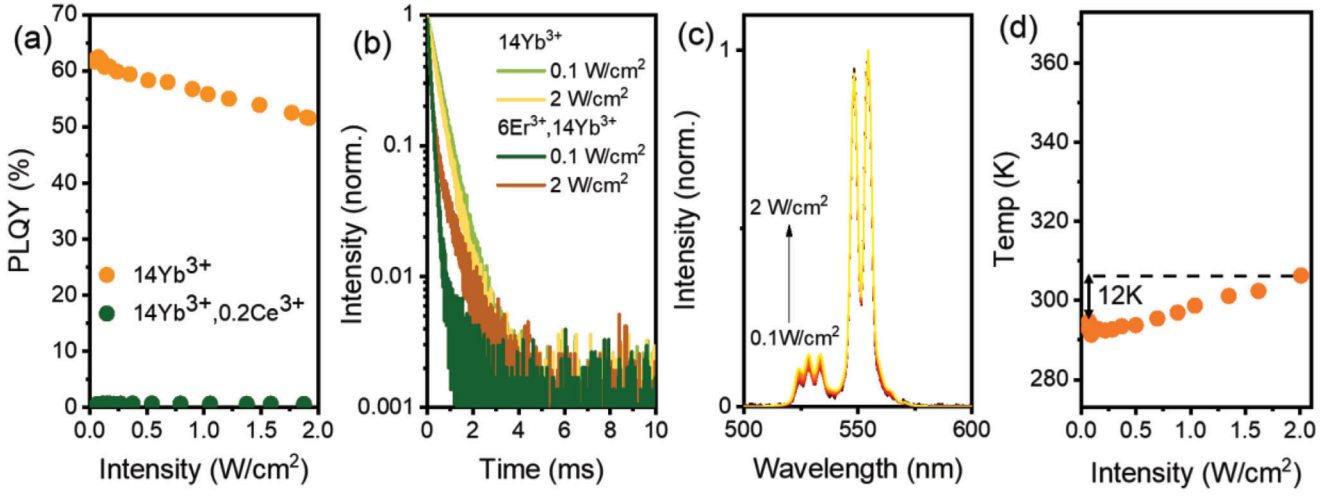

Figure 10. a) PLQY of Yb^{3+}:$^2F_{5/2}$-$^2F_{7/2}$ emission ($PLQY_{2\rightarrow1}$) (integration range 950–1050 nm) as a function of excitation intensity under excitation wavelengths of 940 nm. Samples: Gd_2O_2S:$14Yb^{3+}$ and Gd_2O_2S:$14Yb^{3+}$,$0.2Ce^{3+}$; b) Decays of Yb^{3+}:$^2F_{5/2}$ state and Er^{3+}:$^4H_{11/2}$&Yb^{3+}:$^2F_{5/2}$ manifold in Gd_2O_2S:$14Yb^{3+}$ and Gd_2O_2S:$6Er^{3+}$,$14Yb^{3+}$ samples, respectively, measure at 2 excitation intensities (940 nm) of 0.1 and 2 W cm^{-2}; c) UC spectra in the Gd_2O_2S:$6Er^{3+}$,$14Yb^{3+}$ sample as a function of excitation intensity under 976 nm excitation; d) Temperature of the Gd_2O_2S:$6Er^{3+}$,$14Yb^{3+}$ sample as a function of excitation intensity under 976 nm excitation.

Although the luminescence decays of $Gd_2O_2S:6Er^{3+},14Yb^{3+}$ samples are mostly not applicable in the estimation of efficiency of quenching or ET or internal conversion, it is interesting to look at their behavior. First, a comparison of decays for the $Gd_2O_2S:6Er^{3+},14Yb^{3+}$ sample measured for 2 intensities of 0.1 and 2 W cm^{-2}, demonstrates a significant increase of contribution long-lived component in case of the higher intensity. We assume that the origin of this component is the ETU pathways (with the contribution of both the Er^{3+}:$^4I_{13/2}$ state and the Yb^{3+}:$^2F_{5/2}$&Er^{3+}:$^4I_{11/2}$ manifold) which is realized in the $Gd_2O_2S:6Er^{3+},14Yb^{3+}$ sample with increase of excitation intensity.

Therefore, the unique rise of DS PLQY (**Figure** 6a) in the $Gd_2O_2S:6Er^{3+},14Yb^{3+}$ sample can be also explained via the rise contribution of ETU.

Second, Figure 10b shows the decay behavior of $Gd_2O_2S:14Yb^{3+}$ at both 0.1 and 2 W cm^{-2}. Using the lifetime and PLQY values, we can deduce the radiative rate using Equation 2, which gives 1.27 ms^{-1} (assuming $\beta = 1$) in both cases. Since the radiative rate remains constant, the decrease in $PLQY_{3\rightarrow 5}$ shown in Figure 10a can be attributed solely to the increase in the non-radiative rate probably due to variations in sample temperature. Figure S4b (Supporting Information) shows that irradiation of $Gd_2O_2S:6Er^{3+},14Yb^{3+}$ (at 940 nm) results in emission in the visible spectrum characterized by 2 transitions: Er^{3+}:$^4S_{3/2}$,$^2H_{11/2}$ – $^4I_{15/2}$ (in the range 525–575 nm) and Er^{3+}:$^4F_{9/2}$ – $^4I_{15/2}$ (in the range 650–700 nm). In addition, the $^4S_{3/2}$ and $^2H_{11/2}$ states are thermally coupled so that the intensity of the high energy peak (at 525 nm) increases with temperature while the intensity of the low energy peak (at 550 nm) decreases. Thus, the ratio of their intensities helps to estimate the temperature within the irradiated volume according to Joseph et al.[49] Figure 10c shows the intensity variations for the above peaks, which facilitates temperature calculations. In addition, Figure 10d shows a temperature increase of $\Delta T = 12K$ as the intensity increases from 0.1 to 2 W cm^{-2}. To further investigate the extent of heating in this system, we focused on the excitation beam and measured temperature changes over excitation intensities ranging from 5 to 200 W cm^{-2}. Figure S6 (Supporting Information) demonstrates that the temperature can increase up to 120 °C with increasing excitation intensity.

2.3. XPS Study

As previously described, a pronounced quenching phenomenon of Yb^{3+} was observed in the presence of Ce^{3+} ions, even at a minimal concentration of 0.1 mol.%. The idea that Yb^{3+} is quenched by Ce^{3+} via an electron transfer mechanism is challenging, especially in light of the conventional assumption that the high-energy 4d state of Ce^{3+} is typically quenched by Yb^{3+} via electron transfer.[50] Consequently, we can deduce another quenching mechanism. It is envisaged that during the synthesis of the $Gd_2O_2S:6Er^{3+},14Yb^{3+}$, xCe^{3+} samples using Gd_2O_3, Yb_2O_3, CeO_2, and S with carbon as reducing agent, the presence of both Yb^{2+} and Ce^{4+} oxidation states could occur. The formation of Yb^{2+} ions under synthesis at reducing conditions may be accomplished by the formation of oxygen-based defect states,[51] whereas the presence of non-reduced Ce^{4+} requires charge compensation which can be achieved via Me^{3+} (where Me is Gd, Er, Yb, or Ce) vacancies. These defects could potentially act as quenching centers for the Yb^{3+}:$^2F_{5/2}$ state and reduce the intensity of its luminescence. Excitation of the Yb^{3+}:$^2F_{5/2}$ state is followed by energy migration until it encounters a quenching center.

The presence of distinct valence states of Yb and Ce was confirmed by XPS analysis (**Figure** 11a,b). Previous studies have reported a binding energy difference of ≈8.9 eV between the $4d_{5/2}$ and $4d_{3/2}$ states of Yb^{2+}, accompanied by a peak intensity ratio of 3:2.[52–56] Consequently, the peaks observed ≈181 and 190 eV (Figure 11a) in the spectra are attributed to the $4d_{5/2}$ and $4d_{3/2}$ states of Yb^{2+}, respectively. Furthermore, the presence of an additional 6 peaks in the spectra arises from Yb^{3+} multiplet splitting due to interactions with the 4f energy level.[53]

The Ce3d spectra of cerium compounds consist of 10 peaks, corresponding to the $3d_{5/2}$ (labeled as v) and $3d_{3/2}$ (labeled as u) components with an area ratio of 3:2.[57,58] The peaks labeled as v, v^{II}, v^{III} and u, u^{II}, u^{III} are associated with cerium in the Ce^{4+} species, while v_0, v^{I},u_0, and u^{I} peaks are attributed to cerium in the Ce^{3+} species.[58–61] Figure 11b displays the Ce3d spectrum of the Gd_2O_2S host with different combinations of dopant ions. An increase in intensity is observed in Ce3d spectra due to the increasing amount of cerium and the reliable peak fitting can be applied only to the $Gd_2O_2S:6Er^{3+},14Yb^{3+},5Ce^{3+}$ spectrum. The spin-orbit splitting in all doublets (v_0/u_0, v/u, v′/u′, v^{II}/u^{II}, v^{III}/u^{III}) was set at 18.5 eV, and the full widths at half maximum were kept the same for fitting purposes. The details of the curve fitting results are provided in Table S3 (Supporting Information). At low cerium content (0.2 mol. %), weak intensity peaks observed at the v^{I} (885.4 eV) and u^{I} (904.0) suggest the presence of Ce^{3+}(Figure S7a, Supporting Information). It was observed that at high cerium content, Ce was present in a mixture of oxidation states Ce^{3+}/Ce^{4+}, with the highest intensity peaks being v^{I} and u^{I} corresponding to to Ce^{3+} state. Mixed oxidation states of Ce^{3+}/Ce^{4+} (as well as Yb^{2+}/Yb^{3+}) suggest the presence of oxygen defects.

Figure 11c displays the fits of the oxygen O1s peaks in both the undoped Gd_2O_2S host and the host doped with various elements. In the undoped host material, 3 peaks were observed at 529.3 eV (O1), 531.1 eV (O2), and 532.5 eV (O3). The first 2 peaks can be assigned as lattice oxygen peaks in the Gd_2O_2S.[62] The peak at ≈532 eV may be assigned to chemisorbed species.[63–65] Introduction of dopants into the Gd_2O_2S host results in an increase in the number of observed peaks in the O1s spectrum. Specifically, additional peaks emerge at ≈529 eV (associated with Ce-O bonding states-O4),[66–68] 526.9 eV (Er-O bonding states-O6),[68–70] and 531 eV (Yb-O bonding states-O7)[68,71] (Figure S7b, Supporting Information). Moreover, a peak at ≈530 eV (O5 peak) is observed across different combinations, attributed to a defect peak related to oxygen vacancies of the materials.[65,72–76] As the concentration of Ce dopant increases, both the intensity of the 530 eV (defects) peak and the 529 eV (Ce-O) peaks exhibit enhancement, suggesting a direct relationship between dopant concentration and oxygen defect density. Consequently, quantifying the luminescence quenching caused by these defects can be challenging, but predictive models, such as those proposed by Qin et al.,[48] offer valuable insights into this phenomenon.

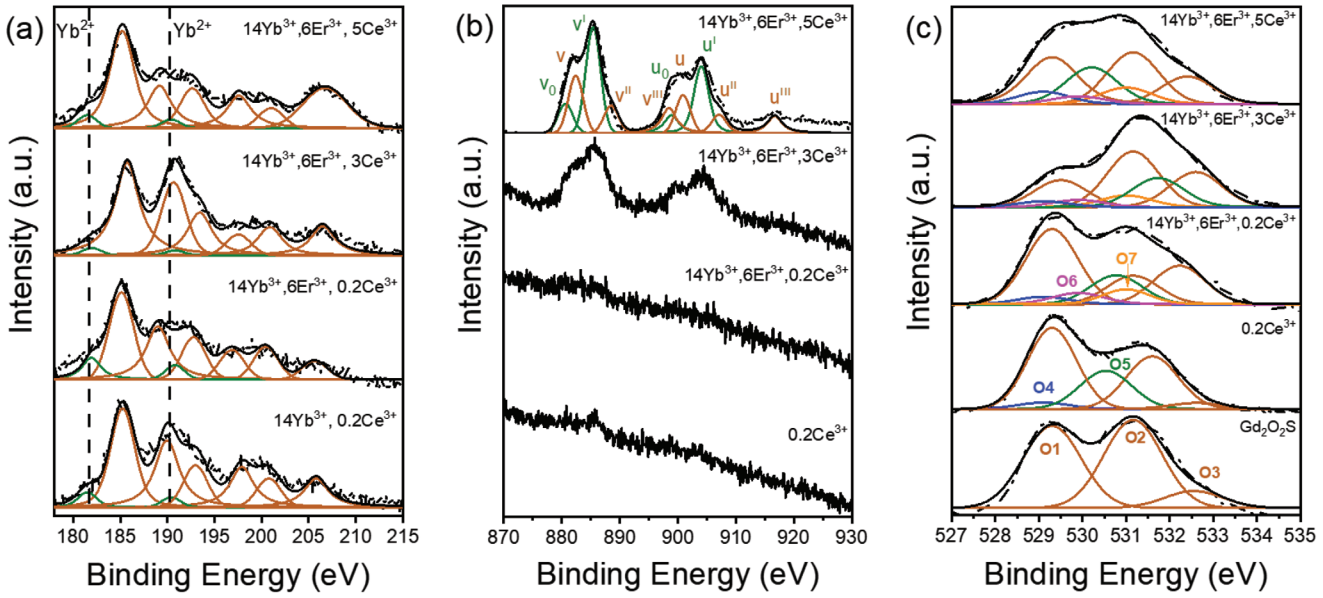

Figure 11. a) Yb 4d XPS spectra of Gd_2O_2S samples co-doped with different combinations of Yb^{3+}, Er^{3+}, and Ce^{3+}. The solid green and brown fitted peak lines represent Yb^{2+} and Yb^{3+} components, respectively. b) Ce 3d XPS spectra of Gd_2O_2S samples co-doped with different combinations of Yb^{3+}, Er^{3+}, and Ce^{3+}. The solid green fitted peak lines represent the Ce^{3+} (v_0, v', u_0, u') and solid brown fitted peak lines represent the Ce $^{4+}$ (v, v'', v''',u, u'', u''') components. c) O 1s XPS spectra of Gd_2O_2S samples co-doped with different combinations of Er^{3+}, Yb^{3+}, and Ce^{3+}. The brown fitted peak lines of Gd_2O_2S are labeled as O1, O2, and O3. The blue and green solid lines are first observed in Gd_2O_2S:0.2Ce^{3+} and labeled as O4 and O5, respectively. The pink and orange solid lines are first observed in Gd_2O_2S:6Er^{3+}, 14Yb^{3+}, 0.2Ce^{3+} and labeled as O6 and O7, respectively. All measured data are represented by black dots, while fitted data are shown as solid lines.

2.4. Generation of Luminescent Codes

In order to test the performance of the studied material a palette of codes with different compositions was prepared and the number of possible luminescent signals was analyzed with a hyperspectral imaging technique. Two sets of mixtures (here and after the word mixture is identical to the word code) were prepared – one had a mixture of Gd_2O_2S:14Yb^{3+}, 6Er^{3+}, and Gd_2O_2S:14Yb^{3+} tracers in different proportions while the second one had a mixture of Gd_2O_2S:14Yb^{3+}, 6Er^{3+}, 0.2Ce^{3+} and Gd_2O_2S:14Yb^{3+} tracers (Figure S8, Supporting Information). The list of all combinations is presented in Table 1. The obtained hyperspectral image is presented in **Figure 12a** and the emission spectra of each mixture are given in Figure 12b,c. To enhance the visualization of the differences in the emission signals of the samples, a pseudo-color image of the test palette depicted in Figure 12a was generated. To compose the image, the intensity in the 1010 nm channel of the hyperspectral camera was used as the Blue channel in the color image, the 1540 nm channel was used as the Green one, and the 1700 nm channel as the Red one. Thus, an increase in the Yb^{3+} emission led to the samples having a more intense blue color, while higher Er^{3+} emission intensity manifested in samples looking greener. Next the intensity ratio of 2 luminescent bands was calculated for each mixture. The luminescent band in the 1000–1200 nm range was considered to originate from Yb^{3+} ions while the luminescent band in the 1400–1700 nm range was considered to originate from Er^{3+} ions. The obtained ratios are presented in Figure 12d. Since the measurement of each luminescence intensity at each detector wavelength can be considered as an uncorrelated value, the uncertainty of the luminescent band integral can be calculated according to the work of Woolliams.[77] Then the uncertainty of the ratio of 2 bands was calculated according to error propagation (see Supporting information section). The calculated uncertainty did not exceed 2% (Table S4, Supporting Information). It should be noted that this level of uncertainty was achieved in a lab under controlled conditions. In a real-world scenario with a much higher scanning speed (3 $m^{-1}s$) and environmental temperature fluctuations inside the sorting facility, the reliability of the reading will decrease. For example, in a

Table 1. Composition of the test palette. Yb stands for the Gd_2O_2S:14Yb^{3+}, ErYb – Gd_2O_2S:14Yb^{3+}, 6Er^{3+} and ErYbCe – Gd_2O_2S:14Yb^{3+}, 6Er^{3+}, 0.2Ce^{3+} sample. The numbers in italics represent the weight fraction of the tracers in the mixture.

	A	C	F	H
11	*0.5*Yb/*0.5*ErYb		*0.5*Yb/*0.5*ErYbCe	
10		*1*ErYb		*1*ErYbCe
9	*0.6*Yb/*0.4*ErYb		*0.6*Yb/*0.4*ErYbCe	
8		*0.1*Yb/*0.9*ErYb		*0.1*Yb/*0.9*ErYbCe
7	*0.7*Yb/*0.3*ErYb		*0.7*Yb/*0.3*ErYbCe	
6		*0.2*Yb/*0.8*ErYb		*0.2*Yb/*0.8*ErYbCe
5	*0.8*Yb/*0.2*ErYb		*0.8*Yb/*0.2*ErYbCe	
4		*0.3*Yb/*0.7*ErYb		*0.3*Yb/*0.7*ErYbCe
3	*0.9*Yb/*0.1*ErYb		*0.9*Yb/*0.1*ErYbCe	
2		*0.4*Yb/*0.6*ErYb		*0.4*Yb/*0.6*ErYbCe
1	*1*Yb			

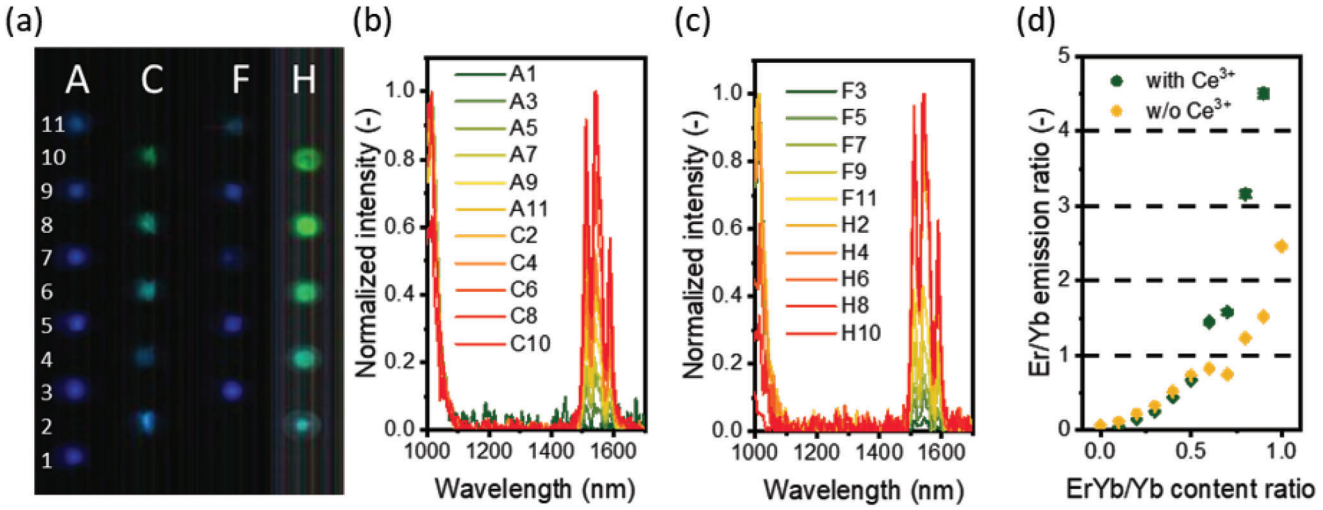

Figure 12. Example of the sorting tracers based on the Gd_2O_2S: Er^{3+}, Yb^{3+}, and Gd_2O_2S:Yb^{3+} phosphors: a) SWIR hyperspectral image. To build pseudo-color intensities at 1010, 1540, and 1700 nm are used as Blue, Green, and Red bands respectively. Normalized emission spectra of the b) 6Er14Yb14/14Yb and c) 6Er14Yb0.2Ce/14Yb sets of samples. d) ratio of the Er^{3+} and Yb^{3+} emission bands.

sorting plant without precise temperature control, the temperature can fluctuate in the average range of 15–30 °C (in Central Europe countries). As a result, the ratiometric signal from luminescent tracers can also change. Figure S9 (Supporting Information) shows the temperature dependence of the ratio between Er^{3+} luminescence in the Gd_2O_2S:14Yb^{3+},6Er^{3+}, 0.2Ce^{3+} sample and Yb^{3+} luminescence in the Gd_2O_2S:14Yb^{3+} sample (normalized so that the ratio is unity at 25 °C). The ratio changes in the range of 1.15–0.94 when the temperature is increased from 15 to 30 °C. This allows reliably differentiating only between intensities that differ by 20% or more. The available range of ratios has therefore been divided into larger 20% increments (corresponding to Er/Yb emission ratios of 1,2...5). With this in mind the mixture that uses the Gd_2O_2S:14Yb^{3+},6Er^{3+} tracer provided only 3 distinguishable intensity ratios, while the mixtures using the Gd_2O_2S:14Yb^{3+},6Er^{3+}, 0.2Ce^{3+} tracer provided 4 different combinations plus one containing only the Gd_2O_2S:14Yb^{3+},6Er^{3+}, 0.2Ce^{3+} tracer (which did not exhibit the Yb^{3+} emission band and is not presented in Figure 12d). This highlights that our assumption presented in Figure 1 is correct and that the addition of Ce^{3+} ions is beneficial as it allows better control of the emission characteristics of the combinations of 2 tracers.

3. Conclusion

In summary, this research significantly expands the range of luminescent tracers with the aim of improving the efficiency of tracer-based sorting of polymer waste. The extension of tracer options has been achieved by combining the single-doped Gd_2O_2S:Yb^{3+} tracer with a novel triply-doped Gd_2O_2S:Yb^{3+},Er^{3+},Ce^{3+} tracer, creating a unique spectral code detectable by SWIR hyperspectral imaging. The use of these tracers in the sorting of plastics enables reliable categorization according to tailored requirements, whether it is to distinguish between food-grade polyethylene terephthalate (such as trays) and its non-food-grade counterparts (such as personal care applications), or even to accurately distinguish between different brands. The uniqueness of the synthesized triply-doped sample is due to several special features. First, it exploits the robust absorption capacity of Yb^{3+} at wavelengths of 940 or 976 nm. Second, the incorporation of Ce^{3+} effectively suppresses the Yb^{3+} luminescence at ≈1000 nm without interfering with the energy transfer from Yb^{3+} to Er^{3+}, thus enhancing the Er^{3+} luminescence at ≈1550 nm. Thirdly, the enhancement of luminescence was quantified by measuring the figure of merit parameter of luminescent tracers – the photoluminescence quantum yield – which showed a remarkable value of 5.7% (for excitation at 940 nm and emission peak at ≈1550 nm). In addition, the specific quenching mechanism of Yb^{3+} in Gd_2O_2S:Yb^{3+}, Er^{3+}, Ce^{3+} tracers is elucidated by XPS analysis, revealing the presence of Yb^{2+}/Ce^{4+} ions acting as quenching centers for the Yb^{3+}:$^2F_{5/2}$ state.

4. Experimental Section

Materials: Gd_2O_3 (ChemPur, purity 99.9%), Yb_2O_3 (ChemPur, purity 99.9%), Er_2O_3 (ChemPur, purity 99.9%), CeO_2 (ChemPur, purity 99.9%), Sulfur (S), (ChemPur, purity 99%), Na_2CO_3 (ChemPur, purity 99%), and K_3PO_4 (ChemPur, purity 99%), were used as a starting material.

Synthesis: A series of Gd_2O_2S 14 mol.% Yb^{3+} 6 mol.% Er^{3+} *x* mol.% Ce^{3+}, where $0 \leq x \leq 5$ mol.% CeO_2 (Gd_2O_2S:6Er^{3+},14Yb^{3+}, *x*Ce^{3+}) samples were synthesized by solid-state flux-assisted technique. The molar ratio of rare earth oxides: Na_2CO_3: K_3PO_4: S = 1: 1.5: 0.5: 8 were weighed respectively, and then homogeneously ground using a mortar and pestle for ≈20 min. Excess sulfur was added to ensure that the oxysulfide formed completely. After thorough mixing, the mixture was transferred to a small covered alumina crucible, which was then placed into a larger alumina crucible containing ≈2 g active carbon to create a reducing atmosphere.[78–80] The covered double alumina crucibles were then placed into a furnace (Thermconcept, KLS-05/13). The firing temperature was set to 1150 °C with an increment of 8 °C min^{-1} for 2 h. Once the samples cooled to room temperature, they were removed from the furnace, washed thoroughly with deionized water 5 times using a centrifuge to remove excess material, and then dried at 150 °C for 2 h. The washing process results in a white powder compared to the yellow powder obtained after the reaction (Figure S10a, Supporting Information). The color change was achieved by the removal of excess flux and sulfur as shown in the XRD spectra for unwashed and washed samples (Figure S10b, Supporting Information). Finally, the

dried powder was ground one last time. Note, that Ce^{3+}-free samples were synthesized using the same heating conditions, but without adding active carbon.

Material Characterisation: Crystal structure analysis and phase identification were performed by using X-ray diffraction (XRD, Bruker, D2 Phaser) equipped with Cu Kα radiation (1.5405 Å), with scanning rate 1 s per step, 0.02° increment, over a 2θ range of 20° to 80°). Rietveld refinements were performed by using TOPAS software and VESTA[81] was used for viewing crystal structures. The synthesized powders' microstructure was imaged using a scanning electron microscope (SEM, Zeiss, SUPRA 60VP) equipped with a SE-II detector. The samples were sputter coated with 10 nm of silver to enhance SEM imaging. Energy dispersive X-ray spectroscopy (EDX) was performed using a Bruker AXS Xflash Detector 5010 and an accelerating voltage of 10 kV.

X-ray photoelectron spectroscopy (XPS) was carried out with the dynamic scanning X-ray photoelectron microprobe (PHI Quantes), having a pass energy of 280 eV, energy steps of 1 eV each increment, and a dwell duration of 100 ms/step for each energy step for Survey scans. The peak fits were done on high-resolution XPS spectra with a pass energy of 26 eV for the host material and 55 eV for the dopants. The energy per step was 0.1 eV and the time per step was 20 ms. The peak fitting was performed using the Fityk[82] software with a Gauss–Lorentz (G–L) function after Shirley background subtraction. The Raman spectrum of samples was recorded using 785 nm excitation and with a 3.5 cm^{-1} resolution (Polytec i-Raman instrument). Elemental analyses were conducted using X-ray fluorescence spectroscopy (XRF; Bruker S8 TIGER).

Optical Characterisation: The diffuse reflectance spectra (DRS) and the absorbance spectra of the samples were obtained using a UV/vis/NIR spectrophotometer (Agilent, Cary 7000) with an integrating sphere module operating in the absorbance mode. The data was presented as $A = \log(\frac{1}{R})$, where R was the reflectance.

The photoluminescent quantum yield (PLQY) – the ratio of the number of photons emitted by a sample compared to the number of absorbed photons – was determined with an optical setup built around an integrating sphere (Labsphere, Ø 6″, 3P-LPM-060-SL). The sample was placed in the middle of a sphere and excited with a continuous-wave laser diode operating either at 940 nm (Thorlabs, M9-940-0200), or 976 nm (Roithner, RLT980-200GS), or 1510 nm (Roithner, RLT1510-15MGS). The laser diodes were mounted on a temperature-controlled mount (Thorlabs, TCLDM9) and driven with a laser diode controller (Thorlabs, ITC4001). The NIR emission bands as well as the intensity of the incident laser were detected with a NIR spectrometer (Ocean Insight, NIRQuest). The emission bands in the visible region were obtained with a visible range spectrometer (Avantes, AvaSpec-ULS2048 × 64TEC-EVO). During the measurement of the laser intensity without the sample the wall of the integrating sphere made of Spectrolon served as the reference. The PLQY was calculated using the 3 M method[83] The luminescence decays were obtained with an infrared single-photon detector (ID Quantique, ID220) coupled to the multi-channel scaling card (TimeHarp 260, Picoquant). The wavelength was selected with a double monochromator (Bentham, DTMS300). The same laser diodes as in the PLQY measurements were used as excitation sources. Photoluminescence excitation spectra (PLE) were obtained with a spectrofluorometer (Edinburgh Instruments, FS5). The hyperspectral data was obtained with a SWIR hyperspectral camera (Specim, SWIR), where a tunable CW Ti:Sapphire laser (M-Squared Lasers Ltd, SolsTiS) operating at 940 nm, pumped by a 532 nm laser (Verdi-V18, Coherent) was used as the excitation source. The laser intensity was 0.5 W cm^{-2} on the sample.

Supporting Information

Supporting Information is available from the Wiley Online Library or from the author.

Acknowledgements

A.C.E. and E.M. contributed equally to this work. The financial support provided by the Helmholtz Association is gratefully acknowledged: i) a Recruitment Initiative Fellowship for B.S.R.; ii) the funding of chemical synthesis equipment from the Helmholtz Materials Energy Foundry (HEMF); and iii) Research Field Energy – Program Materials and Technologies for the Energy Transition – Topic 1 Photovoltaics. B.S.R. and A.T. acknowledge funding from the European Union's Horizon 2020 research and innovation project "Circular Foodpack" agreement No: 101003806.

Open access funding enabled and organized by Projekt DEAL.

Conflict of Interest

The authors declare no conflict of interest.

Data Availability Statement

The data that support the findings of this study are available from the corresponding author upon reasonable request.

Keywords

downshifting quantum yield, lanthanide oxysulfides, luminescence tracers, phosphor, plastic waste recycling, tracer based sorting

Received: April 4, 2024
Revised: June 20, 2024
Published online:

[1] Plastics – The Facts 2022, https://plasticseurope.org/knowledge-hub/plastics-the-facts-2022/, (accessed: January 2024).
[2] EUR-Lex –52018DC0028 – EN; EUR-Lex., https://eur-lex.europa.eu/legal-content/EN/TXT/?uri=COM%3A2018%3A28%3AFIN, (accessed: March 2024).
[3] J. Gasde, J. Woidasky, J. Moesslein, C. Lang-Koetz, *Sustainability* **2021**, *13*, 258.
[4] S. Brunner, P. Fomin, C. Kargel, *Waste Manage.* **2015**, *38*, 49.
[5] K. Rajagopalan, E. Madirov, D. Busko, I. A. Howard, B. S. Richards, H. C. Swart, A. Turshatov, *ACS Appl. Mater. Interfaces* **2023**, *15*, 43985.
[6] J. Tan, S. Jia, S. Ramakrishna, *Processes* **2023**, *11*, 1457.
[7] E. Brown, A. MacDonald, S. Allen, D. Allen, *J. Hazardous Mater. Adv.* **2023**, *10*, 100309.
[8] M. J. Stapleton, A. J. Ansari, A. Ahmed, F. I. Hai, *Sci. Total Environ.* **2023**, *902*, 166090.
[9] J. Woidasky, I. Sander, A. Schau, J. Moesslein, P. Wendler, D. Wacker, G. Gao, D. Kirchenbauer, V. Kumar, D. Busko, I. A. Howard, B. S. Richards, A. Turshatov, S. Wiethoff, C. Lang-Koetz, *Resour., Conserv. Recycl.* **2020**, *161*, 104976.
[10] C. Olscher, A. Jandric, C. Zafiu, F. Part, *Polymers* **2022**, *14*, 3074.
[11] G. Gao, A. Turshatov, I. A. Howard, D. Busko, R. Joseph, D. Hudry, B. S. Richards, *Adv. Sustainable Syst.* **2017**, *1*, 1600033.
[12] I. A. Howard, D. Busko, G. Gao, P. Wendler, E. Madirov, A. Turshatov, J. Moesslein, B. S. Richards, *Resour., Conserv. Recycl.* **2024**, *205*, 107557.
[13] R. Martín-Rodríguez, S. Fischer, A. Ivaturi, B. Froehlich, K. W. Krämer, J. C. Goldschmidt, B. S. Richards, A. Meijerink, *Chem. Mater.* **2013**, *25*, 1912.
[14] B. Lei, Y. Liu, J. Zhang, J. Meng, S. Man, S. Tan, *J. Alloys Compd.* **2010**, *495*, 247.
[15] S. A. Osseni, S. Lechevallier, M. Verelst, C. Dujardin, J. Dexpert-Ghys, D. Neumeyer, M. Leclercq, H. Baaziz, D. Cussac, V. Santran, R. Mauricot, *J. Mater. Chem.* **2011**, *21*, 18365.
[16] B. Ortega-Berlanga, L. Betancourt-Mendiola, C. del Angel-Olarte, L. Hernández-Adame, S. Rosales-Mendoza, G. Palestino, *Crystals* **2021**, *11*, 1094.

[17] Y. V. Orlovskii, T. T. Basiev, K. K. Pukhov, M. V. Polyachenkova, P. P. Fedorov, O. K. Alimov, E. I. Gorokhova, V. A. Demidenko, O. A. Khristich, R. M. Zakalyukin, *J. Lumin.* **2007**, *125*, 201.
[18] S. He, X. Zhao, M. C. Tan, *RSC Adv.* **2017**, *7*, 35738.
[19] V. Kataria, D. S. Mehta, *J. Phys. D: Appl. Phys.* **2018**, *51*, 145501.
[20] M. Xing, L. Kang, X. Wu, T. Pang, H. Wang, Y. Fu, X. Luo, Y. Tian, *Dalton Trans.* **2021**, *50*, 13468.
[21] Y. Song, Y. Huang, L. Zhang, Y. Zheng, N. Guo, H. You, *RSC Adv.* **2012**, *2*, 4777.
[22] V. Kataria, S. Dixit, D. S. Mehta, *J. Mater. Sci.* **2019**, *54*, 13635.
[23] X. Li, L. Lu, H. Sun, X. Zhang, Z. Bai, X. Mi, *ECS J. Solid State Sci. Technol.* **2020**, *9*, 106001.
[24] I. P. Machado, J. de Wit, A. J. van Bunningen, C. C. S. Pedroso, L. C. V. Rodrigues, H. F. Brito, A. Meijerink, *J. Alloys Compd.* **2023**, *942*, 169083.
[25] X. Gong, Y. Chen, Y. Lin, J. Huang, Z. Luo, Y. Huang, *J. Appl. Phys.* **2010**, 108.
[26] J. Xu, L. Su, H. Li, D. Zhang, L. Wen, H. Lin, G. Zhao, *Optical Mater.* **2007**, *29*, 932.
[27] X. Liu, J. Qiu, X. Xu, D. Zhou, *J. Nanosci. Nanotechnol.* **2016**, *16*, 3749.
[28] E. Sani, A. Toncelli, M. Tonelli, *Optical Mater.* **2006**, *28*, 1317.
[29] B. Huang, Y. Zhou, F. Yang, L. Wu, Y. Qi, J. Li, *Optical Mater.* **2016**, *51*, 9.
[30] A. De Martinis, L. Montalto, L. Scalise, D. Rinaldi, P. Mengucci, C. Michail, G. Fountos, N. Martini, V. Koukou, I. Valais, A. Bakas, C. Fountzoula, I. Kandarakis, S. David, *Crystals* **2022**, *12*, 854.
[31] R. Fernández-González, J. J. Velázquez, V. D. Rodríguez, F. Rivera-López, A. Lukowiak, A. Chiasera, M. Ferrari, R. R. Gonçalves, J. Marrero-Jerez, F. Lahoz, P. Núñez, *RSC Adv.* **2016**, *6*, 15054.
[32] X. Gao, X. Liu, Q. Wen, X. Yang, S. Xiao, *J. Appl. Phys.* **2014**, 116.
[33] A. N. Georgobiani, V. B. Gutan, M. A. Kazaryan, A. V. Krotov, O. Y. Manashirov, Y. P. Timofeev, *Inorg. Mater.* **2009**, *45*, 1166.
[34] J. H. Huang, Y. J. Chen, X. H. Gong, Y. F. Lin, Z. D. Luo, Y. D. Huang, *J. Opt. Soc. Am. B* **2010**, *27*, 2605.
[35] E. Sani, A. Toncelli, M. Tonelli, D. A. Lis, E. V. Zharikov, K. A. Subbotin, V. A. Smirnov, *J. Appl. Phys.* **2005**, 97.
[36] Y. H. Tsang, D. J. Binks, B. D. O. Richards, A. Jha, *Laser Phys. Lett.* **2011**, *8*, 729.
[37] Y. Zhang, Y. Shi, Z. Qin, M. Song, W. Qin, *Nanomaterials* **2018**, *8*, 615.
[38] S. Zheng, Y. Zhou, D. Yin, X. Xu, Y. Qi, S. Peng, *J. Quant. Spectrosc. Radiat. Transfer* **2013**, *120*, 44.
[39] G. A. Kumar, M. Pokhrel, A. Martinez, R. C. Dennis, I. L. Villegas, D. K. Sardar, *J. Alloys Compd.* **2012**, *513*, 559.
[40] E. I. Madirov, S. V. Kuznetsov, V. A. Konyushkin, D. Busko, B. S. Richards, A. Turshatov, *Adv. Opt. Mater.* **2024**, 2303094.
[41] R. Shannon, *Acta Crystallogr. A* **1976**, *32*, 751.
[42] M. Ichikawa, Y. Ishikawa, T. Wakasugi, K. Kadono, *J. Mater. Res.* **2010**, *25*, 2111.
[43] G. Yao, C. Lin, Q. Meng, P. Stanley May, M. T. Berry, *J. Lumin.* **2015**, *160*, 276.
[44] D. K. Sardar, W. M. Bradley, J. J. Perez, J. B. Gruber, B. Zandi, J. A. Hutchinson, C. W. Trussell, M. R. Kokta, *J. Appl. Phys.* **2003**, *93*, 2602.
[45] T. Miyakawa, D. L. Dexter, *Phys. Rev. B* **1970**, *1*, 2961.
[46] W. Zheng, H. Zhu, R. Li, D. Tu, Y. Liu, W. Luo, X. Chen, *Phys. Chem. Chem. Phys.* **2012**, *14*, 6974.
[47] D. Yu, T. Yu, A. J. van Bunningen, Q. Zhang, A. Meijerink, F. T. Rabouw, *Light: Sci. Appl.* **2020**, *9*, 107.
[48] X. Qin, L. Shen, L. Liang, S. Han, Z. Yi, X. Liu, *J. Phys. Chem. C* **2019**, *123*, 11151.
[49] R. E. Joseph, D. Busko, D. Hudry, G. Gao, D. Biner, K. Krämer, A. Turshatov, B. S. Richards, I. A. Howard, *Optical Mater.* **2018**, *82*, 65.
[50] D. C. Yu, F. T. Rabouw, W. Q. Boon, T. Kieboom, S. Ye, Q. Y. Zhang, A. Meijerink, *Phys. Rev. B* **2014**, *90*, 165126.
[51] T. Yang, H. Jiang, O. Hai, Y. Dong, S. Liu, S. Gao, *Inorg. Chem.* **2021**, *60*, 17797.
[52] B. Morkoç, A. Kahraman, E. Yılmaz, *J. Mater. Sci.: Mater. Electron.* **2021**, *32*, 9231.
[53] M. Y. A. Yagoub, H. C. Swart, E. Coetsee, *Phys. B* **2023**, *669*, 415298.
[54] S. J. Crerar, A. Mar, A. P. Grosvenor, *J. Solid State Chem.* **2012**, *196*, 79.
[55] A. Kahraman, H. Karacali, E. Yilmaz, *J. Alloys Compd.* **2020**, *825*, 154171.
[56] M. Y. A. Yagoub, H. C. Swart, E. Coetsee, *Mater. Res. Bull.* **2017**, *93*, 170.
[57] M. Romeo, K. Bak, J. El Fallah, F. Le Normand, L. Hilaire, *Surf. Interface Anal.* **1993**, *20*, 508.
[58] A. Pfau, K. D. Schierbaum, *Surf. Sci.* **1994**, *321*, 71.
[59] E. Paparazzo, *J. Phys.: Condens. Matter* **2018**, *30*, 343003.
[60] K. A. Litvintseva, Y. A. Chesalov, A. V. Selivanova, A. A. Saraev, V. V. Kaichev, *J. Phys. Chem. C* **2024**, *128*, 3193.
[61] A. P. Sefage, M. A. Mamo, P. L. Masiteng, A. Balakrishna, E. Coetsee, H. C. Swart, L. Reddy, *Phys. B* **2022**, *647*, 414383.
[62] J. J. Dolo, H. C. Swart, J. J. Terblans, E. Coetsee, O. M. Ntwaeaborwa, B. F. Dejene, *Phys. B* **2012**, *407*, 1586.
[63] M. A. Naghmash, M. M. Ibrahim, *Mater. Chem. Phys.* **2022**, *283*, 126036.
[64] S. K. S. Patel, P. Dhak, M.-K. Kim, J.-H. Lee, M. Kim, S.-K. Kim, *J. Magn. Magn. Mater.* **2016**, *403*, 155.
[65] V. Kumar, H. C. Swart, O. M. Ntwaeaborwa, R. E. Kroon, J. J. Terblans, S. K. K. Shaat, A. Yousif, M. M. Duvenhage, *Mater. Lett.* **2013**, *101*, 57.
[66] M. Aslam, I. M. I. Ismail, S. Chandrasekaran, T. Almeelbi, A. Hameed, *RSC Adv.* **2014**, *4*, 49347.
[67] T. L. Barr, C. G. Fries, F. Cariati, J. C. J. Bart, N. Giordano, *J. Chem. Soc. Dalton Trans.* **1983**, https://doi.org/10.1039/DT98300018251825.
[68] Y. Uwamino, T. Ishizuka, H. Yamatera, *J. Electron Spectrosc. Relat. Phenom.* **1984**, *34*, 67.
[69] S. Kaya, E. Yilmaz, *Nucl. Instr. Meth. Phys. Res. Sect. B: Beam Interact. Mater. Atoms* **2018**, *418*, 74.
[70] F. H. Chen, J. L. Her, Y. H. Shao, Y. H. Matsuda, T. M. Pan, *Nanoscale Res. Lett.* **2013**, *8*, 18.
[71] B. D. Padalia, W. C. Lang, P. R. Norris, L. M. Watson, D. J. Fabian, W. C. Price,Proc. R. Soc. A Math. Phys. Eng. Sci. **1977**, *354*, 269.
[72] A. Rawat, S. Panwar, L. P. Purohit, *Surf. Interf.* **2023**, *42*, 103404.
[73] R. Zou, K. Xu, T. Wang, G. He, Q. Liu, X. Liu, Z. Zhang, J. Hu, *J. Mater. Chem. A* **2013**, *1*, 8560.
[74] S. Kalasina, K. Kongsawatvoragul, N. Phattharasupakun, P. Phattharaphuti, M. Sawangphruk, *RSC Adv.* **2020**, *10*, 14154.
[75] A. Sahai, N. Goswami, *Ceram. Int.* **2014**, *40*, 14569.
[76] C. Hu, Y. Huang, R. Rao, *Appl. Surf. Sci.* **2023**, *635*, 157671.
[77] E. R. Woolliams, National Physical Laboratory, **2013**.
[78] L. Feng, Y. Tian, L. Wang, C. e. Cui, Q. Shi, P. Huang, *J. Mater. Sci.* **2016**, *51*, 2841.
[79] H.-W. Wei, L.-M. Shao, H. Jiao, X.-P. Jing, *Optical Mater.* **2018**, *75*, 442.
[80] C. Guo, H. Jing, T. Li, *RSC Adv.* **2012**, *2*, 2119.
[81] K. Momma, F. Izumi, *J. Appl. Crystallogr.* **2011**, *44*, 1272.
[82] M. Wojdyr, *J. Appl. Crystallogr.* **2010**, *43*, 1126.
[83] J. C. de Mello, H. F. Wittmann, R. H. Friend, *Adv. Mater.* **1997**, *9*, 230.